Increased Heat Risk in Wet Climate Induced by Urban Humid Heat

Keer Zhang[1], Chang Cao[2,3], Haoran Chu[2,3], Lei Zhao[4], Jiayu Zhao[2,5], Xuhui Lee[1]

[1]School of the Environment, Yale University, New Haven, CT 06511, USA

[2]Center on Atmospheric Environment, International Joint Laboratory on Climate and Environment Change (ILCEC), Nanjing University of Information Science and Technology, Nanjing 210044, China

[3]Key Laboratory of Meteorological Disaster, Ministry of Education and Collaborative Innovation Center on Forecast and Evaluation of Meteorological Disasters, Nanjing University of Information Science and Technology, Nanjing 210044, China

[4]Department of Civil and Environmental Engineering, University of Illinois at Urbana-Champaign, Urbana, IL 61801, USA.

[5]College of Ocean and Meteorology, Guangdong Ocean University, Zhanjiang 524088, China

Correspondence to: Xuhui Lee (xuhui.lee@yale.edu)

Summary

Cities are generally warmer than their adjacent rural land, a phenomenon known as the urban heat island (UHI). Often accompanying the UHI is another phenomenon called the urban dry island (UDI) whereby humidity in urban land is lower than that in their surroundings[1–3]. The UHI exacerbates heat stress on urban residents[4,5], while the UDI may instead provide relief because the human body can cope with hot conditions better at lower humidity through perspiration[6,7]. The relative balance between UHI and UDI – as measured by changes in wet-bulb temperature (T_w) – is a key yet largely unknown determinant of human heat stress in urban climates. Here we show that T_w is reduced in cities in dry and moderately wet climates, where the UDI more than offsets the UHI, but increased in wet climates (summer precipitation P_s > 570 mm). Our results arise from analysis of urban and rural weather stations across the world and calculations with an urban climate model. In wet climates, the urban daytime T_w is 0.17 ± 0.14 °C (mean ± 1 standard deviation) higher than rural T_w in the summer, primarily because of a weaker dynamic mixing in urban air. This T_w increment is small, but because of high background T_w in the wet climate, it is enough to cause two to six extra dangerous heat-stress days per summer for urban residents under current climate conditions. The risk of extreme humid heat is projected to increase in the future, and these urban effects may further amplify the risk.

Introduction

Time of the day and time of the year matter in the examination of urban heat stress. Air temperature and air humidity are more likely to exceed dangerous heat stress thresholds in the daytime and during the summer because of higher background temperature and humidity than at night and during the winter. The UDI can bring more cooling relief if it occurs during summer daylight hours. How the UDI interacts with the UHI has important health implications, especially in cities in the Global South. Some of these cities are home to informal settlements with low access to air conditioning infrastructure and vulnerable to temperature extremes[8–10], and many are located in tropical and subtropical climates where the combined effect of high temperature and high humidity is approaching the human physiological threshold for survival (T_w = 35 °C)[11,12]. A strong UDI in these cities may have the potential to fully compensate for the adverse UHI effect. On the other hand, if these cities are more humid than their rural background, the high humidity will compound high urban temperatures, pushing heat stress levels even closer to the lethal threshold.

Current knowledge of these urban microclimate effects is limited[13,14] for high heat-stress regions in humid climates, such as South Asia, the Tropical Africa, and the Amazon Basin[11,12]. Satellite data show that the daytime surface UHI (urban-rural difference in land surface temperature) is stronger in more humid climate[15,16]. One underlying mechanism is that cities in humid climates are less efficient in dissipating heat from the surface to the lower atmosphere than the surrounding rural land[15,17]. A working hypothesis is that the low convection efficiency of urban land should also enhance the daytime air UHI intensity (urban-rural difference in air temperature) in humid climates.

Reduction in urban evaporation due to vegetation removal is a key mechanism of the UDI formation[3]. The UDI phenomenon has been observed in several mid-latitude cities[18-20] in background climates where evaporation is water-limited. But in low-latitude humid climate where evaporation is energy-limited, urban air may become more moist than the rural background[21,22]. It is not known if these local results can be extended to broader geographic regions.

In this study, we investigate the contributions of the UHI and the UDI to urban heat stress using 133 pairs of urban and rural stations across the world. We also used an urban climate model to simulate the UHI and the UDI for over 36,000 urban clusters in the world, with the goals to expand the spatial coverage of the observational data and to probe the thermodynamic mechanisms of UHI and UDI formation. Results are presented for the three summer months. We use the wet-bulb temperature (T_w) to measure the combined effect of temperature and humidity on heat stress. Because it is the lowest temperature that can be achieved by evaporation of water in an air parcel, T_w is a good approximation of the skin temperature of a cloth-less and perspiring human body. This approximation may be more appropriate in hot and humid climates than in dry or cold climates. We find that the urban humid heat burden is dependent on precipitation regime.

The urban wet-bulb island

We investigate the urban effects using the urban wet-bulb island, ΔT_w, defined as the difference in T_w between the urban and the adjacent rural land (urban minus rural). Mathematically, ΔT_w is the sum of the scaled UHI (ΔT_a, °C) and UDI intensity ($\Delta e_a / \gamma$, °C):

$$\Delta T_w = w_1 \Delta T_a + w_2 \frac{\Delta e_a}{\gamma} \quad (1)$$

where w_1 and w_2 are positive and dimensionless scaling factors, ΔT_a and Δe_a are urban-rural differences in air temperature and in vapour pressure, respectively, and γ is the psychrometric constant (Methods). In this formulation, the two scaling factors are equal (at about 0.3, Extended Data Table 1) and are a weak function of T_w. The second term in equation (1) is negative for a city with an UDI and positive if the city is more humid than its surrounding (that is, the urban moist island). Other heat indices can also be expressed as a linear combination of the UHI and the UDI components (Methods).

The paired daytime (08:00 to 16:00 local time) observations show that, on average, the negative UDI contribution (that is, the urban dry island) outweighs the positive UHI contribution in dry (P_s < 180 mm) and moderately wet (intermediate P_s from 180 to 570 mm) climates, resulting in negative ΔT_w (Fig. 1a). In other words, cities in these climates experience less humid heat stress in the daytime than their rural environments. In wet climate (P_s > 570 mm), the average UDI contribution is near zero, and the daytime mean ΔT_w is slightly positive. At night (20:00 to 04:00 local time), the UDI effect is weak, but the UHI effect is strong, leading to positive ΔT_w in all the three climates (Fig. 1c). These observational patterns are reproduced by the climate model (Fig. 1b, d). It is difficult to draw firm conclusions for the wet climate from the observational data because of large variations among the few station pairs (17) available. If we replace the model results for the 17 grids where these station pairs are located with those for all the 10,288 urban clusters in the wet climate, we obtain a mean daytime ΔT_w of 0.17 ± 0.14 °C (mean ± 1 standard deviation), which is significantly different from zero (p < 0.001).

The urban wet-bulb island is a city-scale property. Because most of the observations were made with a single pair of stations, some of the variability in Fig. 1a & c is caused by the inability of a single urban station to capture intra-city variations of microclimate. By applying a bootstrap method to the few cities with multiple station pairs, we estimate that the measurement uncertainty of ΔT_w is 0.12 to 0.57 ^{o}C (95% confidence interval; Table 1).

Causes of the urban wet-bulb island

We use the climate model to quantify causes of the urban wet-bulb island. In the modelling framework, the screen-height T_w is allowed to vary between urban and rural subgrid tiles within the same model grid – this difference is the urban wet-bulb island ΔT_w – and T_w at the atmospheric reference height (i.e. blending height) of the land model is kept constant between these tiles. The wet-bulb temperature T_w measures the surface moist static energy (MSE)[23,24]. Even though MSE (and hence T_w) is a conserved quantity in the adiabatic process, ΔT_w is generally nonzero and is linked to the contrast in the surface enthalpy flux between the urban and the rural tiles.

Using an Ohm's Law analogy for the enthalpy flux (equation 7, Methods), we show that ΔT_w is caused by two diabatic processes: (1) dynamic mixing of air between the screen height and the blending height, and (2) a thermodynamic contribution or diabatic heating due to absorption of solar radiation, anthropogenic heat emission, heat storage in soil and buildings, and surface longwave radiation (Methods; Fig. 2 and Extended Data Fig. 5). Their contributions to ΔT_w are quantified with a diagnostic analysis of model results. During the daytime, changes in dynamic mixing cause the urban T_w to be 0.39 ± 0.34 °C (mean ± 1 SD) higher than the rural T_w in the wet

climate, resulting in a positive ΔT_w (Fig. 2a). In this climate zone, cities dissipate the surface MSE to the lower atmosphere less efficiently than rural landscapes, which are dominated by dense vegetation of high aerodynamic roughness. The mean daytime diffusion resistance r_a between the screen height and the blending height is 20 s m^{-1} and 12 s m^{-1} for urban and rural land, respectively, in the wet climate. This interpretation is consistent with an attribution analysis of the surface UHI[15]. At night, the role of dynamic mixing is reversed: the surface air over urban land is statically more unstable[25,26], permitting more efficient energy dissipation than over rural land (e.g., urban r_a = 72 s m^{-1} versus rural r_a = 91 s m^{-1} in the wet climate), which explains the negative contribution to ΔT_w (Fig. 2b). Despite this dynamic cooling effect, the nighttime ΔT_w is actually positive due to diabatic heating. Diabatic heating, primarily via the release of heat stored in buildings, increases the MSE of urban air at night in all the three climate zones (Fig. 2b).

The paired observations suggest that the urban web-bulb island may be dependent on climate wetness, with the daytime ΔT_w increasing and the nighttime ΔT_w decreasing with increasing summer precipitation (Fig. 1a, c). This climate dependence is more evident in the spatial distributions of modelled ΔT_w (Fig. 3a, c). The spatial variations in dynamic mixing are the dominant driver of spatial variations in the daytime ΔT_w, explaining 130% of the ΔT_w versus precipitation spatial covariance (Extended Data Fig. 4a; ref[15]). At night, diabatic heating via heat stored in soil and buildings is dominant, explaining 125% of the ΔT_w - precipitation covariance (Extended Data Fig. 4b). Both are associated with the background biogeography in that vegetation tends to be denser as the climate becomes wetter, which enhances the daytime rural convection efficiency and suppresses the role of heat storage at night.

The urban dry island in wet and dry climates

Both the observational and the modelling data show that the daytime UDI is stronger in the dry climate (that is, a more negative UDI component) than in the wet climate (Fig. 1a & b; Fig. 4). Although the above diagnostic analysis cannot differentiate the UDI and the UHI components, a similar reasoning can be deployed to explain this UDI climate gradient. First, if a stronger dynamic mixing occurs over urban areas than over rural areas, water vapour released from the urban surface will dissipate faster to the upper boundary layer, leading to the UDI formation. In the modelling domain, mixing is indeed stronger for urban (mean daytime r_a = 14 s m^{-1}) than for rural areas (r_a = 18 s m^{-1}) in the dry climate. Second, reduction in the urban water vapour source due to removal of vegetation, which is akin to reduction in diabatic heating for T_w, is a known contributor to the UDI[3]. In addition, many cities in the dry climate are surrounded by irrigated cropland. Cropland irrigation humidifies the rural air via surface evaporation, further strengthening the UDI. We hypothesize that these changes in the surface vapour sources create a stronger UDI in the dry climate because surface evaporation is water-limited than in the wet climate where surface evaporation is energy-limited.

The occurrence of strong UDIs in the dry climate is somewhat counterintuitive because some greenspaces in arid cities are irrigated (e. g, urban lawns and parks in Salt Lake City, USA[40]). In our model domain, the irrigation option is activated for cropland but not for urban land. The urban weather stations we used are located in built-up neighborhoods (impervious surface fraction greater than 0.45, Methods), so the humidifying effect of urban greenspaces is minimal.

Increased urban heat stress in wet climate

That the daytime ΔT_w is more likely to be positive than negative in the wet climate (Fig. 3) is a cause of concern. Because the summer daytime wet-bulb temperature in the wet climate is already quite high (mean daytime T_w 25.4 ± 2.5 °C), especially in coastal areas (mean daytime T_w 26.2 ± 1.9 °C), even a small increase in T_w can create large negative health consequences. Using a dangerous T_w threshold of 27 °C (ref[12,28,29]), we find that residents in coastal cities in the wet climate experience, on average, 5.6 more dangerous days per summer (ΔN) than rural residents during 2000 to 2019 ($p < 0.001$; Fig. 5a). In several cities, the extra urban heat burden can be as high as 20 days per summer. The number of extra dangerous days is lower (2.4) for interior cities, but it is still significantly different from zero ($p < 0.001$).

At night, the urban wet-bulb island is less a concern (Fig. 5b), even though ΔT_w is larger than the daytime ΔT_w (Fig. 3). The mean nighttime T_w (22.7 ± 2.9 °C) in the wet climate is much lower than the 27 °C threshold.

Discussion

The results presented above offer partial support for the convection efficiency hypothesis. The daytime convection efficiency of urban land becomes lower than rural land in a wetter climate, so more MSE is trapped in the urban surface air, leading to a more positive ΔT_w (Fig. 1a & b, Extended Data Fig. 4a). But this hypothesis alone cannot fully explain the air UHI spatial pattern, which shows higher values in a drier climate in an opposite trend to ΔT_w (ED Fig. 2c).

The relationship between the air UHI and precipitation is complex. A negative correlation of the air UHI with climate wetness has been reported in ref[30] and is suggested by the air UHI dependence on latitude[31]. Other authors have reported insignificant[13] or positive correlation[32].

The divergence among these studies is probably caused by large intracity variations in the observed air temperature or uncertainties related to model representation of rural irrigation.

Although our urban climate model does not explicitly consider urban vegetation, some inferences can be made from the above thermodynamic insights regarding the use of vegetation for adaptation to humid heat. Urban vegetation can reduce air temperature by promoting evaporation, increasing albedo, and changing heat storage[33]. Evaporation on its own does not play a role in the formation of the urban wet-bulb island since it merely converts sensible heat to latent heat, bringing no change to the total MSE. The cooling relief of vegetation to humid heat is likely achieved via other biophysical changes. Urban vegetation may be beneficial at night because diabatic heating via heat storage is the main contributor to the nighttime urban wet-bulb island (Fig. 2). In Seoul, South Korea, street trees at a fractional cover of 30% reduce the nighttime heat storage by about 15 W m^{-2} (ref[34]), which amounts to a reduction of about 0.30 °C in T_w according to our diagnostic analysis. A less studied effect of urban vegetation is change to dynamic mixing. According to the data from urban microclimate model simulations[27,35], planting of street trees reduces air temperature but raises air humidity, with the overall result being increases in T_w. One reason is that in the model domain, the urban landscape becomes aerodynamically smoother with increasing tree cover[36]. Heat dissipation is controlled by thermal roughness, not by momentum roughness. Rigid structures such as buildings have much lower thermal roughness than flexible and porous plant foliage[37,38]. It is not known if the thermal roughness of a complex urban landscape consisting of built structures and street vegetation will behave in the same way as its momentum roughness.

Our study highlights the need to consider the combined urban temperature and humidity effect on human health. This effect is generally omitted in the existing global and regional studies on humid heat because they are based either on historical climate data collected mostly at rural weather stations or on reanalysis data products and future climate projections that lack urban representation. The urban effect is dependent on local and regional background climate conditions (Figs. 3 and 5). In the dry and intermediate climates, the UDI is strong enough to more than offset the UHI in many locations, but there is no reduction in the average heat burden for urban residents. In the wet climate, the urban effect increases the number of dangerous heat stress days by 2.4 to 5.6 per summer, an intensification that is greater than the humid heat burden of 0.5 ± 0.3 days from widespread irrigation in this region[29]. The humid heat stress is projected to increase under future warmer climates, and the urban wet-bulb island may further exacerbate the problem in some regions. In the western Maritime Continent (Malaysia, Indonesia, Singapore, and Brunei), about 2% of the population is projected to be at risk of experiencing extreme humid heat (T_w greater than 32 °C) at the end of the century under the RCP8.5 scenario[39]. In this region, the daytime ΔT_w is 0.33 °C (Fig. 3a, top panel). Using the cumulative exposure probability in ref[39], addition of this urban effect to the projected T_w would increase the at-risk population to 4%.

REFERENCES

1. Oleson, K. W. et al. Interactions between urbanization, heat stress, and climate change. *Clim. Change* **129**, 525–541 (2015).

2. Luo, M. & Lau, N. C. Urban Expansion and drying climate in an urban agglomeration of East China. *Geophys. Res. Lett*. **46**, 6868–6877 (2019).

3. Meili, N., Paschalis, A., Manoli, G. & Fatichi, S. Diurnal and seasonal patterns of global urban dry islands. *Environ. Res. Lett*. **17**, 054044 (2022).

4. Santamouris, M. Recent progress on urban overheating and heat island research. Integrated assessment of the energy, environmental, vulnerability and health impact. Synergies with the global climate change. *Energy Build*. **207**, 109482 (2020).

5. Ward, K., Lauf, S., Kleinschmit, B. & Endlicher, W. Heat waves and urban heat islands in Europe: A review of relevant drivers. *Sci. Total Environ*. **569–570**, 527–539 (2016).

6. Epstein, Y. & Moran, D. S. Thermal comfort and the heat stress indices. *Ind. Health* **44**, 388–398 (2006).

7. Sherwood, S. C. & Huber, M. An adaptability limit to climate change due to heat stress. *Proc. Natl. Acad. Sci. U. S. A*. **107**, 9552–9555 (2010).

8. Borg, F. H. et al. Climate change and health in urban informal settlements in low- and middle-income countries–a scoping review of health impacts and adaptation strategies. *Glob. Health Action* **14**, 1908064 (2021).

9. Ramsay, E. E. et al. Chronic heat stress in tropical urban informal settlements. *iScience* **24**, 103248 (2021).

10. Revi, A. et al. Urban areas. In: Climate Change 2014: Impacts, Adaptation, and Vulnerability. in Climate Change 2014: Impacts, Adaptation, and Vulnerability. Part A: Global and Sectoral Aspects. *Contribution of Working Group II to the Fifth Assessment Report of the Intergovernmental Panel on Climate Change* 535–612 (Cambridge University Press, 2014).

11. Raymond, C., Matthews, T. & Horton, R. M. The emergence of heat and humidity too severe for human tolerance. *Sci. Adv*. **6**, eaaw1838 (2020).

12. Im, E.-S., Pal, J. S. & Eltahir, E. A. B. Deadly heat waves projected in the densely populated agricultural regions of South Asia. *Sci. Adv*. **3**, e1603322 (2017).

13. Du, Y. et al. 2021. Simultaneous investigation of surface and canopy urban heat islands over global cities. *ISPRS J. Photogram. Remote Sensing* **181**, 67–83 (2021).

14. Stewart, I. D. A systematic review and scientific critique of methodology in modern urban heat island literature. *Int. J. Climatol*. **31**, 200–217 (2011).

15. Zhao, L., Lee, X., Smith, R. B. & Oleson, K. Strong contributions of local background climate to urban heat islands. *Nature* **511**, 216–219 (2014).

16. Manoli, G. et al. Magnitude of urban heat islands largely explained by climate and population. *Nature* **573**, 55–60 (2019).

17. Fitria, R., Kim, D., Baik, J. & Choi, M. Impact of biophysical mechanisms on urban heat island associated with climate variation and urban morphology. *Sci. Rep*. **9**, 19503 (2019).

18. Lee, D. O. Urban-rural humidity differences in London. *Int. J. Climatol*. **11**, 577–582 (1991).

19. Holmer, B. & Eliasson, I. Urban-rural vapour pressure differences and their role in the development of urban heat islands. *Int. J. Climatol*. **19**, 989–1009 (1999).

20. Kuttler, W., Weber, S., Schonnefeld, J. & Hesselschwerdt, A. Urban/rural atmospheric water vapour pressure differences and urban moisture excess in Krefeld, Germany. *Int. J. Climatol*. **27**, 2005–2015 (2007).

21. Wang, Z., Song, J., Chan, P. W. & Li, Y. The urban moisture island phenomenon and its mechanisms in a high-rise high-density city. *Int. J. Climatol*. **41**, E150–E170 (2020).

22. Shi, Y. & Zhang, Y. Urban morphological indicators of urban heat and moisture islands under various sky conditions in a humid subtropical region. *Build. Environ*. **214**, 108906 (2022).

23. Zhang, Y. & Fueglistaler, S. How Tropical convection couples high moist static energy over land and ocean. *Geophys. Res. Lett*. **47**, 1–8 (2020).

24. Zhang, Y., Held, I. & Fueglistaler, S. Projections of tropical heat stress constrained by atmospheric dynamics. *Nat. Geosci*. **14**, 133–137 (2021).

25. Dupont, E., Menut, L., Carissimo, B., Pelon, J. & Flamant, P. Comparison between the atmospheric boundary layer in Paris and its rural suburbs during the ECLAP experiment. *Atmos. Environ.* **33**, 979–994 (1999).

26. Oke, T. R. The energetic basis of the urban heat island. *Q. J. R. Meteorol. Soc*. **108,** 1–24 (1982).

27. Meili, N. et al. An urban ecohydrological model to quantify the effect of vegetation on urban climate and hydrology (UT&C v1.0). *Geosci. Model Dev*. **13**, 335–362 (2020).

28. Mishra, V. et al. Moist heat stress extremes in India enhanced by irrigation. *Nat. Geosci*. **13**, 722–728 (2020).

29. Krakauer, N. Y., Cook, B. I. & Puma, M. J. Effect of irrigation on humid heat extremes. *Environ. Res. Lett*. **15**, 094010 (2020).

30. Liu, Y. et al. Urban heat island effects of various urban morphologies under regional climate conditions. *Sci. Total Environ*. **743**, 140589 (2020).

31. Wienert, U. & Kuttler, W. The dependence of the urban heat island intensity on latitude - A statistical approach. *Meteorol. Zeitschrift* **14**, 677–686 (2005).

32. Zhang, Z., Paschalis, A., Mijic, A., Meili, N., Manoli, G., van Reeuwijk, M., & Fatichi, S. A mechanistic assessment of urban heat island intensities and drivers across climates. *Urban Climate* **44**, 101215 (2022).

33. Wong, N. H., Tan, C. L., Kolokotsa, D. D. & Takebayashi, H. Greenery as a mitigation and adaptation strategy to urban heat. *Nat. Rev. Earth Environ*. **2**, 166–181 (2021).

34. Lee, S. H. et al. Impacts of in-canyon vegetation and canyon aspect ratio on the thermal environment of street canyons: numerical investigation using a coupled WRF-VUCM model. *Q. J. R. Meteorol. Soc*. **142**, 2562–2578 (2016).

35. Huang, X., Song, J., Wang, C., Chui, T. F. M. & Chan, P. W. The synergistic effect of urban heat and moisture islands in a compact high-rise city. *Build. Environ*. **205**, 108274 (2021).

36. Meili, N. et al. Tree effects on urban microclimate: Diurnal, seasonal, and climatic temperature differences explained by separating radiation, evapotranspiration, and roughness effects. *Urban For. Urban Green*. **58**, 126970 (2021).

37. Voogt, J. A. & Grimmond, C. S. B. Modeling surface sensible heat flux using surface radiative temperatures in a simple urban area. *J. Appl. Meteorol*. **39**, 1679–1699 (2000).

38. Li, Q., Bou-Zeid, E., Grimmond, S., Zilitinkevich, S. & Katul, G. Revisiting the relation between momentum and scalar roughness lengths of urban surfaces. *Q. J. R. Meteorol. Soc*. **146**, 3144–3164 (2020).

39. Im, E. S., Kang, S. & Eltahir, E. A. B. Projections of rising heat stress over the western Maritime Continent from dynamically downscaled climate simulations. *Glob. Planet. Change* **165**, 160–172 (2018).

40. Gómez-Navarro, C., D. E. Pataki, E. R. Pardyjak, & D. R. Bowling. Effects of vegetation on the spatial and temporal variation of microclimate in the urbanized Salt Lake Valley. *Agric. For. Meteorol*. **296**, 108211 (2021).

Table 1 | Uncertainties in the observed urban wet-bulb island (ºC) caused by intra-city microclimate variability. CI: 95% confidence interval; S.E.: standard error of bootstrap sampling.

City	Phoenix	Harrisburg	Birmingham	Guangzhou[20]
Climate zone	Dry	Inter.	Inter.	Wet
	Daytime			
CI	(-1.20, -0.68)	(-0.49, -0.12)	(-0.05, 0.07)	(0.39, 0.65)
S.E.	0.20	0.09	0.03	0.07
	Nighttime			
CI	(-0.19, 0.38)	(0.68, 1.00)	(0.50, 0.63)	(0.97, 1.22)
S.E.	0.19	0.09	0.03	0.07

FIGURE LEGENDS

Fig. 1 | The urban wet-bulb island depends on time of the day and on climate wetness. a, c, Observed daytime (a) and nighttime (c) ΔT_w and its components; b, d, Modelled daytime (b) and nighttime (d) ΔT_w and its components. Model results are for grids corresponding to the urban-rural station pairs and from the same time periods. Box plots show the median (line), 25-75% range (box), 5-95% range (whiskers), and the mean value (cross).

Fig. 2 | The urban wet-bulb island is controlled by dynamic mixing and diabatic heating. The results of diagnostic analysis during the daytime (a) and nighttime (b). The modelled ΔT_w is difference in T_w between urban and rural subgrid tiles in the same model grid. The calculated ΔT_w is the sum of all component contributions. Box plots show the median (line), 25-75% range (box), 5-95% range (whiskers), and the mean value (cross).

Fig. 3 | The daytime urban wet-bulb island is strongest in the wet climate. a, b, Geographical distributions of ΔT_w during daytime (a) and nighttime (b) in three climate zones. c, d, Probability density function of daytime (c) and nighttime ΔT_w (d). Box and whiskers show 1, 25, 50, 75 and 99 percentiles. Maps were made with the Python software.

Fig. 4 | The modelled daytime UDI component is more negative (stronger UDI) with decreasing summer precipitation. Each data bin consists of 1819 grids. Box plots show the median (line), 25-75% range (box), 5-95% range (whiskers), and the mean value (cross).

Fig. 5 | Urban residents in the wet climate experience more heat-stressed days than rural residents. The daytime (a) and nighttime (b) heat stress burden caused by the urban wet-bulb island. ΔN is difference in the number of heat-stressed days per summer between urban and rural locations. Results are shown separately for coastal and interior cities in three climate regions. Color indicates data density, with yellow indicating high density and navy blue low density. Smooth curves are probability density functions. Box and whiskers show 0, 25, 50, 75, and 100 percentiles.

METHODS

The results presented here are for the summer season (JJA of the northern hemisphere and DJF of the southern hemisphere). These months represent the hot period of the year and also coincide with high-humidity conditions in the wet season at low latitudes. For grids north of 20° N, the highest T_w always occurs in June, July, or August. For grids south of 18° S, the hottest month (month with the highest T_w) is always December, January, or February. The T_w seasonality is weaker in the tropics (between 18° S to 20° N) than at mid- to high latitudes. The hottest month can be March or April in some grid cells between 0° and 18° S and May or September in some grid cells between 0° and 20° N. On average, JJA in the Northern Hemisphere and DJF in the Southern Hemisphere are the hottest period of the year at these tropical latitudes.

We used summer precipitation P_s to divide observations and model grids into wet (P_s > 570 mm), dry (P_s < 180 mm) and intermediate (180 mm < P_s < 570 mm) climate regions; these three regions roughly coincide with the tropical, dry, and temperate & boreal climate in the Köppen climate classification. Coastal grids are defined as those within 50 km from coasts of oceans and large lakes. The daytime and nighttime periods are 08:00 to 16:00 and 20:00 to 04:00 local time.

Selection of paired urban-rural weather stations

Some studies have used data collected at municipal airports as a substitute for urban conditions. This practice is controversial. Consideration of turbulent mixing in the atmospheric boundary layer indicates that weather stations have a small source footprint on the order of 500 m in radius[41]. Because airport weather stations are generally in compliance with the World Meteorological Organization siting guideline (which stipulates that a weather station be installed

on an open ground covered by grass and the location should be far away from buildings and walls), they may not be representative of the true built environment.

Here, we applied a set of uniform site selection criteria to ensure that the chosen stations are located in true buildup and true rural landscapes. First, the paired stations have simultaneous observations of both temperature and humidity at hourly or 3-hourly intervals for at least one summer from 2009 to 2019.

Second, station location and measurement height are within our pre-set standards. One challenge about climate data depositories is that the accuracy of station coordinates is generally no better than one arcminute or about 2 km in distance. Because of the heterogenous nature of urban environments, a 2-km spatial ambiguity means that a station classified as urban in a medium or small city can actually be located in a rural setting. We verified the metadata for each site pair with the site operator or via visual inspection of the station location using Google Earth Pro. This screening ensures that the accuracy of the station coordinates is better than 200 m and that temperature and humidity sensors are placed at a height of 1.3 to 3 m above the surface.

Third, we used the GHS built-up grid data[42] to screen potential urban and rural weather stations, after their precise station coordinates had been confirmed. Stations with a built-up fraction higher than 0.45 within the 1-km radius were chosen as urban, and stations with a built-up fraction lower than 0.2 within the 3-km radius were chosen as rural. These buffers are greater than the theoretical footprint of about 500-m radius for a weather station[41]. The buffer for screening urban stations is smaller than for rural stations, allowing us to include urban stations in small cities.

Fourth, the elevation difference, absolute distance, and latitudinal distance between the paired stations are smaller than 100 m, 80 km, and 50 km, respectively. A small lapse rate correction (-0.0065 °C m^{-1}) was applied to remove the impact of the residual elevation difference.

A total of 133 urban-rural station pairs were found to satisfy the above screening criteria, including 101 from the intermediate climate, 17 from the wet climate, and 15 from the dry climate (Extended Data Fig. 1). Of these, 45 stations came from the Integrated Surface Database[43] and the rest were extracted from local sources and from intensive field campaigns. If a model grid has multiple station pairs, spatial average of urban stations and spatial average of rural station are used to form one single pair for that grid.

Climate model simulation

We used a global climate model, the Community Earth System Model (CESM)[44], to simulate urban and rural wet-bulb temperature and other surface climate variables. The land component of CESM, the Community Land Model Version 5 (CLM5), represents subgrid spatial heterogeneity with five land units or tiles (glacier, lake, urban, vegetated, and crop). The land units in the same grid cell receive identical atmospheric forcing, but their physical state and flux variables are computed separately with their own parameterizations. For instance, the urban microclimate is based on the urban canyon concept, which consists of roof, sunlit wall, shaded wall, and pervious and impervious canyon floor. The urban extent, urban morphology, and thermal and radiative parameters come from a default urban dataset provided by CESM[45], representing the present-day urbanization pattern. In this modelling framework, the urban wet-bulb island (ΔT_w) is the T_w

difference between the urban and the rural (vegetated and crop) land units in the same grid cell. Because CLM5 does not consider the lateral heat and moisture transport between the rural and urban land units, the modelled urban-rural microclimate gradients may be biased high in magnitude for small cities. The wet-bulb temperature at the atmospheric reference height (i.e. blending height) of the land model is kept constant between these land units. This configuration is similar to the tropical atmosphere where the surface climate can vary between the land and the ocean, but the MSE (and hence T_w) is horizontally uniform in the free troposphere[23]. There, the weak regional T_w gradient is maintained by deep moist convection[23,46]. In the local-scale study presented here, the uniform T_w at the atmospheric reference height represents the effect of horizontal blending of air due to turbulent eddies in the lower atmospheric boundary layer[47].

Cropland irrigation can influence urban-rural microclimatic gradients[48]. If moisture in the topsoil of the crop land unit falls below a pre-set threshold, irrigation water is added until soil moisture reaches field capacity. Timing of the daily peak T_w is not sensitive to irrigation. In grid cells in Northern India subject to irrigation, both urban and rural maximum T_w occur at around 13:00 to 14:00 local time.

The model simulation was forced by the ERA5-Land hourly data[49] at the finest spatial resolution (25 km) configured for CESM. The model was first run for 10 years driven by the ERA climatology from 2000 to 2009. After this spin-up, it was run for another 20 years, driven by the ERA forcing data from 2000 to 2019. Post-simulation analysis was based on hourly model outputs. This 20-year period encompasses all the paired weather station observations.

The model has reproduced the observed day-versus-night contrast in ΔT_w and the ΔT_w climate gradient (Fig. 1). Other studies have also reported good performance of the same modelling system in simulating the surface urban heat island[15] and urban air temperature[50].

In Extended Data Fig. 6, we compare observed and modelled diurnal patterns of T_w, the urban wet-bulb island, and its UHI and UDI components for Berlin, Germany (in the intermediate climate zone) and Phoenix, USA (in the dry climate zone). We chose these two cities because there are multiple rural and urban stations. These station mesonets allow a total of 4 and 6 possible urban versus rural pairings for Berlin and Phoenix, respectively. The larger diurnal amplitude of the modelled T_w than that of the observed T_w is primarily caused by high amplitude biases of air temperature and humidity in the forcing data. Overall, the model has reproduced the observed diurnal patterns in urban-rural differences in T_w, air temperature and humidity.

In the wet climate zone, the observations are available only as one pair per city. Furthermore, observational hours vary among these sites. The most common observation hours are 2:00, 8:00, 14:00 and 20:00 local time. (Out of the 17 pairs, 11 have observations at these hours.) These are used for comparison with the model data (Extended Data Fig. 7). Both model and observational data indicate weak diurnal patterns in urban-rural differences in T_w, air temperature and humidity, which is consistent with the results shown in the main text (Fig. 1).

Separating the urban wet-bulb island into UHI and UDI components

The wet-bulb temperature of the environment is measured with a wet-bulb thermometer, a thermometer wrapped in wet cloth and in well-ventilated conditions. The latent heat of

evaporation of the wet bulb is balanced by sensible heat from the environment. This energy balance consideration is the basis of the wet-bulb equation[51]:

$$T_w + \frac{e_s^*(T_w)}{\gamma} = T_a + \frac{e_a}{\gamma} \quad (2)$$

where T_w and T_a are wet-bulb temperature and air temperature, respectively, e_a and e_s^* are actual and saturation vapour pressure, respectively, and γ is the psychrometric constant. Equation (2) expresses T_w as an implicit function of T_a and e_a. Differentiating equation (2) and using a linear approximation to e_s^*, we obtain equation (1). The scaling factors in equation (1) are given by:

$$w_1 = w_2 = 1/(1 + \frac{\Delta_w}{\gamma}) \quad (3)$$

where Δ_w is the slope of the saturation vapour pressure at T_w. The accuracy of equation (1) is better than 0.017 °C for 95% of the urban clusters in comparison with ΔT_w obtained from a numerical solution of equation (2). The global maps of the UDI and the UHI components are shown in Extended Data Fig. 2c-f.

Diagnostic analysis of the urban wet-bulb island

Wet-bulb temperature and equivalent temperature (T_q) both measure the MSE. Their relationships can be expressed as[52]

$$T_q = T_a + \frac{e_a}{\gamma} = T_w + \frac{e_s^*(T_w)}{\gamma} \quad (4a,b)$$

The surface-to-air enthalpy flux is driven by the vertical gradient of T_q. To show this, we first apply an Ohm's law analogy to the sensible (H) and latent heat flux (λE) as

$$H = \rho c_p \frac{T_a - T_b}{r_a} \tag{5}$$

$$\lambda E = \lambda \rho \frac{q_a - q_b}{r_a} \tag{6}$$

where q is specific humidity, ρ is air density, λ is latent heat of vaporization, c_p is specific heat of air at constant pressure, r_a is diffusion resistance, and subscripts a and b denote the screen height and the blending height, respectively. Using equations 4a, 5 and 6, we obtain an expression for the enthalpy flux

$$H + \lambda E = \rho c_p \frac{T_{q,a} - T_{q,b}}{r_a} \tag{7}$$

In this equation, the surface enthalpy flux ($H + \lambda E$) is proportional to the difference in equivalent temperature between the screen height and the blending height and is inversely proportional to the diffuse resistance between the two heights.

The surface energy balance equation is

$$R_n + Q_A = H + \lambda E + G \tag{8}$$

where Q_A is anthropogenic heat flux, and G is heat storage flux. The net radiation R_n is given by

$$R_n = (1 - \alpha) K_{\downarrow} + L_{\downarrow} - L_{\uparrow} \tag{9}$$

where α is albedo, $K_{\downarrow}$ and $L_{\downarrow}$ are the downward solar radiation and longwave radiation, respectively, and $L_{\uparrow}$ is the upward longwave radiation.

Combining equations (7) and (8), we obtain a solution for the screen-height equivalent temperature,

$$T_{q,a} = T_{q,b} + \frac{r_a(R_n + Q_A - G)}{\rho c_p} \quad (10)$$

Differentiating equation (4b) and making use of equation (10) and the fact that the blending-height equivalent temperature $T_{q,b}$ is constant between the urban and the rural subgrid tiles in the same model grid, we obtain a diagnostic equation for the urban wet-bulb island,

$$\Delta T_w = \frac{1}{\rho c_p(1 + \Delta_w/\gamma)}[\Delta r_a (R_n + Q_A - G) + r_a \Delta(R_n + Q_A - G)] \quad (11)$$

where Δ_w is the slope of saturation vapour pressure at T_w and Δ is a spatial difference operator (urban minus rural). The first term in the square brackets on the right-hand side of equation (11) represents the contribution to ΔT_w from urban-rural difference in dynamic mixing, and the second term is the contribution from diabatic heating difference. The diabatic contribution is further partitioned into components associated with the anthropogenic heat flux, the absorbed solar radiation, the heat storage flux and the surface longwave radiation.

The diagnostic analysis was performed with subgrid data generated by the climate model at hourly time steps and averaged to the daytime (08:00 to 16:00) and the nighttime period (20:00 to 04:00). The diffusion resistance was obtained from the following diagnostic relationship,

$$r_a = \frac{\rho c_p(T_{q,a} - T_{q,b})}{H + \lambda E} \quad (12)$$

Other variables were computed directly by the model. In the model, $K_{\downarrow}$, $L_{\downarrow}$, and $T_{q,b}$ are the same between the urban and the rural sub-grid tiles in a model grid. The credibility of this analysis is supported by the good agreement between modelled ΔT_w and ΔT_w calculated as the sum of component contributions (Extended Data Fig. 3; Fig. 2).

Comparison of heat stress indices

Similar to equation (1), the urban-rural difference in an empirical heat stress index can be decomposed mathematically into a temperature and a humidity component, in the following general form,

$$\Delta\text{Heat Index} = w_1 \Delta T_a + w_2 \frac{\Delta e_a}{\gamma} \quad (13)$$

But the scaling factors w_1 and w_2 differ from those for the urban wet-bulb island. For example, the wet-bulb globe temperature (WBGT) is a linear combination of T_w and T_a,

$$\text{WBGT} = 0.7T_w + 0.3T_a \quad (14)$$

Making use of equations (1), (3), and (14), the scaling factors for WBGT are

$$w_1 = \frac{0.7}{1 + \Delta_w/\gamma} + 0.3;\ w_2 = \frac{0.7}{1 + \Delta_w/\gamma} \quad (15)$$

The Heat Index is a nonlinear function of temperature and humidity[53]. Its scaling factors were obtained numerically. The results are summarized in Extended Data Table 1.

In the present study, T_w is used as the measure of humid heat stress which has equal weights on air temperature and humidity. Other heat stress indices weigh temperature more heavily than humidity (Extended Data Table 1). The urban heat stress will be stronger than our assessment if these indices are used. Although a meta analysis of mortality data clearly demonstrates the importance of humidity[54], epidemiological studies generally do not show strong evidence for the humidity effect (e. g., ref[55]). In the real world, heat stress is also influenced by other factors, such as wind speed, radiation and physical activities. A condition implicit in the wet-bulb equation is that the human body is cloth-less, resting in the shade, and the skin is fully covered by sweat. We suggest that T_w may be more appropriate for cities in hot and humid climates, where the wet-bulb condition is more likely met, than in dry or cold climates.

Uncertainty analysis

The UHI, the UDI and the wet-bulb island are city-wide properties. Because the observation in most cities was made with only one pair of sites, the observed ΔT_w is subject to uncertainty arising from intra-city variations in microclimate. In several cities, observations are available from multiple pairs of sites. These are used to estimate the measurement uncertainty. The standard deviation of ΔT_w is 0.27 ^{o}C for Berlin, Germany (4 possible urban-rural combinations of site pairing) and 0.30 ^{o}C for Phoenix, USA (6 combinations; Extended Data Fig. 6). By applying a bootstrap sampling to the cities with more than three site pairs and with the data reported for Guangzhou, China[22] (a city in the wet climate zone), we estimate that the measurement uncertainty of ΔT_w is 0.12 to 0.57 ^{o}C (95% confidence interval; Table 1). We added Guangzhou in this analysis because the wet cities in our own dataset are equipped with only one site pair per city. The reader should be aware that the Guangzhou data were collected in the autumn season (September to November), so the intra-city variability is only an approximation of summer conditions.

In some UHI studies, the UHI intensity is calculated as the difference in the daily maximum temperature between urban and rural land. To determine if the results in Fig. 1 are influenced by the timing of maximum T_w, we have calculated the urban wet-bulb island as the urban daily maximum T_w minus the rural daily maximum T_w. The results, given in Extended Data Fig. 8, are nearly identical to those based on daytime mean values (Fig. 1 a & b). For example, the mean modelled ΔT_w is 0.14 °C for the wet climate using this new procedure and that from Fig. 1b is 0.08 °C.

The small number of station pairs for the wet and the dry climate is a limitation of this study. To test the sensitivity to precipitation thresholds, we first changed the dry threshold by 40 mm from 180 mm to 140 mm and 220 mm. The observed dry-climate mean ΔT_w is -0.12 ºC (daytime) and 0.48 ºC (nighttime) with the 140 mm threshold and -0.04 ºC (daytime) and 0.64 ºC (nighttime) with the 220 mm threshold. The original dry-climate mean ΔT_w is -0.05 ºC (daytime) and 0.65 ºC (nighttime; Fig. 1a & c). Next, we adjusted the wet threshold by 40 mm from the original 570 mm to 530 mm and 610 mm. The observed wet-climate mean ΔT_w is -0.10 ºC (daytime) and 0.19 ºC (nighttime) with the 530 mm threshold and 0.02 ºC (daytime) and 0.30 ºC (nighttime) with the 610 mm threshold. The original wet-climate mean ΔT_w is 0.03 ºC (daytime) and 0.28 ºC (nighttime; Fig. 1a &c). These responses are small. The day-versus-night contrast and the climate wetness gradient are unaffected by these threshold changes.

To quantify the uncertainties of ΔT_w due to random omission of cities, we randomly sampled 75% of the site pairs in each of the three categories. This process was repeated 1000 times. The resulting statistics are given in Extended Data Fig. 9. In about 4/5 of the cases, the daytime mean ΔT_w is positive in the wet region and negative in the dry region. At night, the mean ΔT_w is always positive. This sensitivity analysis suggests that we are likely to get statistically significant daytime results if more site pairs are available in the wet region.

DATA AVAILABILITY STATEMENT

The ERA5-Land hourly data is available at:

https://cds.climate.copernicus.eu/cdsapp#!/dataset/reanalysis-era5-land-monthly-means?tab=overview; The GHS built-up grid data at: https://ghsl.jrc.ec.europa.eu/download.php; The ISD data at: https://www.ncei.noaa.gov/access/search/data-search/global-hourly; The observation data from Arizona mesonet at: https://cals.arizona.edu/AZMET/az-data.htm; The observation data from Birmingham Urban Climate Laboratory at: https://catalogue.ceda.ac.uk/uuid/e448a957fc53401794e48a23c265c25f; The observation data from Trans-African Hydro-Meteorological Observatory (TAHMO) at: https://tahmo.org/climate-data/; The observation data obtained from open data portals provided by the National Meteorological Service of different countries are available at: https://www.dwd.de/EN/climate_environment/cdc/cdc_node_en.html (Germany); https://en.ilmatieteenlaitos.fi/download-observations (Finland); https://www.smhi.se/data/meteorologi/ladda-ner-meteorologiska-observationer#param=airtemperatureInstant,stations=core (Sweden); https://www.met.no/en/free-meteorological-data (Norway); https://climate.weather.gc.ca/index_e.html (Canada); https://www.smn.gob.ar/descarga-de-datos (Argentina); https://www.data.jma.go.jp/gmd/risk/obsdl/index.php (Japan); https://portal.inmet.gov.br/dadoshistoricos (Brazil); https://climatologia.meteochile.gob.cl/application/requerimiento/producto/RE3003 (Chile). The data on observed daytime and nighttime Tw and the UHI and UDI components are available on Figshare (https://figshare.com/s/d13cb1c4dd5d056192c9). The hourly model outputs are available from the authors upon request.

CODE AVAILABILITY STATEMENT

The Community Earth System Model Version 2 is available at https://www.cesm.ucar.edu/models/cesm2/. The python code used to produce the figures in this paper is available on Figshare (https://figshare.com/s/d13cb1c4dd5d056192c9).

METHODS REFERENCES

41. Oke, T. R. Initial guidance to obtain representative meteorological observations at urban sites. *Instruments Obs. Methods* (WMO/TD-No. 1250) (2006).

42. Corbane, C., Florczyk, A., Pesaresi, M., Politis, P. & Syrris, V. GHS-BUILT R2018A - GHS built-up grid, derived from Landsat, multitemporal (1975-1990-2000-2014). *European Commission, Joint Research Centre (JRC)* at https://doi.org/10.2905/jrc-ghsl-10007 (2018).

43. Smith, A., Lott, N. & Vose, R. The integrated surface database: Recent developments and partnerships. *Bull. Am. Meteorol. Soc*. **92**, 704–708 (2011).

44. Danabasoglu, G. et al. The Community Earth System Model Version 2 (CESM2). J. *Adv. Model. Earth Syst*. **12**, 1–35 (2020).

45. Jackson, T. L., Feddema, J. J., Oleson, K. W., Bonan, G. B. & Bauer, J. T. Parameterization of urban characteristics for global climate modeling. *Ann. Assoc. Am. Geogr*. **100**, 848–865 (2010).

46. Byrne, M. P. & O'Gorman, P. A. Land-ocean warming contrast over a wide range of climates: Convective quasi-equilibrium theory and idealized simulations. *J. Clim*. **26**, 4000–4016 (2013).

47. Mahrt, L. The bulk aerodynamic formulation over heterogeneous surfaces. *Bound-Layer Meteorol*. **78**, 87–119 (1996).

48. Kumar, R. et al. Dominant control of agriculture and irrigation on urban heat island in India. *Sci. Rep*. **7**, 14054 (2017).

49. Muñoz-Sabater, J. et al. ERA5-Land: A state-of-the-art global reanalysis dataset for land applications. *Earth Syst. Sci. Data* **13**, 4349–4383 (2021).

50. Zhao, L. et al. Global multi-model projections of local urban climates. *Nat. Clim. Change* **11**, 152–157 (2021).

51. Lee, X. *Fundamentals of Boundary- Layer Meteorology*. (Cham, Switzerland : Springer, 2018).

52. Fischer, E. M. & Knutti, R. Robust projections of combined humidity and temperature extremes. *Nat. Clim. Change* **3**, 126–130 (2013).

53. Buzan, J. R., Oleson, K. & Huber, M. Implementation and comparison of a suite of heat stress metrics within the Community Land Model version 4.5. *Geosci. Model Dev*. **8**, 151–170 (2015).

54. Mora, C. et al. Global risk of deadly heat. *Nat. Clim. Change* **7**, 501-506 (2017).

55. Armstrong, B. et al. (2019). The role of humidity in associations of high temperature with mortality: a multicountry, multicity study. *Environ. Health Persp*. **127**, 097007 (2017).

Acknowledgements

CC acknowledges support by the National Key R&D Program of China (grant 2019YFA0607202), XL and LZ by the US National Science Foundation (grants 1933630 & 2145362), LZ by the Institute for Sustainability, Energy and Environment, and KZ by a Yale Graduate Fellowship. High-performance computing support from Cheyenne (https://doi.org/10.5065/D6RX99HX) was provided by NCAR's Computational and Information Systems Laboratory, sponsored by the US National Science Foundation. We thank the following institutions and network operators for providing observation data: U.S. National Centers for Environmental Information, Oklahoma mesonet, Arizona mesonet, Professor Timothy Hawkins, U.S. Environmental Protection Agency, DWD Climate Data Center of Germany, Reliable Prognosis, Trans-African Hydro-Meteorological Observatory (TAHMO), Birmingham Urban Climate Lab, and The National Meteorological Service of Swizerland, France, United Kingdom,

Finland, Sweden, Austria, Spain, Norway, Canada, South Africa, Argentina, Japan, Brazil, Mexico, Chile, China, and Thailand.

Author contributions X.L. designed the research and developed the theory. K.Z. conducted the model simulations and data analysis. K.Z., C.C, H.C., and J.Z. contributed to the observation data collection. L.Z. contributed ideas to the model simulation and data analysis. X.L. and K.Z. drafted the manuscript. All authors edited and revised the manuscript.

Competing interests. The authors declare no competing interests.

EXTENDED DATA LEGENDS

Extended Data Fig. 1 | Distribution of urban-rural station pairs. Base map shows summer precipitation. Map was made with the Python software.

Extended Data Fig. 2 | The urban wet-bulb island and its UHI and UDI components. a, c, e, Daytime distributions; b, d, f, Nighttime distributions. Zonal mean values are also shown. Maps were made with the Python software.

Extended Data Fig. 3 | The urban wet-bulb island calculated with the diagnostic analysis agrees with modelled results. Comparison of modelled and calculated daytime (a) and nighttime (b) urban wet-bulb island. The calculated ΔT_w is the sum of all component contributions. Each data point represents one grid-cell mean value. Color indicates data density. The black dotted line is 1:1. The solid line is linear regression with regression statistics noted.

Extended Data Fig. 4 | The daytime ΔT_w increases and the nighttime ΔT_w decreases with precipitation. a, Daytime; b Nighttime. Data are bin averages. Each bin consists of 1819 grids.

Extended Data Fig. 5 | The heat storage term dominates the diabatic heating contribution to the urban wet-bulb island. The four components of diabatic heating term during the daytime (a) and nighttime (b). Box plots show the median (line), 25-75% range (box), 5-95% range (whiskers), and the mean value (cross).

Extended Data Fig. 6 | Comparison of observed and modelled diurnal patterns of wet-bulb temperature, the urban wet-bulb island, and its UHI and UDI components. a-d, Berlin; d-f, Phoenix. Red filled areas denote one standard deviation of all urban-rural combinations of site pairing.

Extended Data Fig. 7 | Comparison of observed and modelled diurnal patterns of wet-bulb temperature, the urban wet-bulb island, and its UHI and UDI components in the wet climate zone. Gray areas denote one standard deviation of 11 model grids. Error bars denote one standard deviation of 11 site pairs.

Extended Data Fig. 8 | Regional patterns of the urban wet-bulb island and its UHI and UDI components calculated from daily maximum T_w. a, observed; b, modelled. Box plots show the median (line), 25-75% range (box), 5-95% range (whiskers), and the mean value (cross).

Extended Data Fig. 9 | Statistics from random omission of site pairs. a, observed daytime; c, observed nighttime; b, modelled daytime; d, modelled nighttime ΔT_w and its components. Box plots show the median (line), 25-75% range (box), 5-95% range (whiskers), and the mean value (cross).

Extended Data Table 1 | Empirical heat indices weigh temperature more heavily than humidity. Results are presented separately for daytime and nighttime in three climate regions. w_1 – temperature weighting factor, w_2 – humidity weighting factor, T_w – wet-bulb temperature, Humidex – humidity index, WBGT – wet-bulb globe temperature, DI – discomfort index, HI – Heat Index. The heat stress index formulae are given in ref[53]

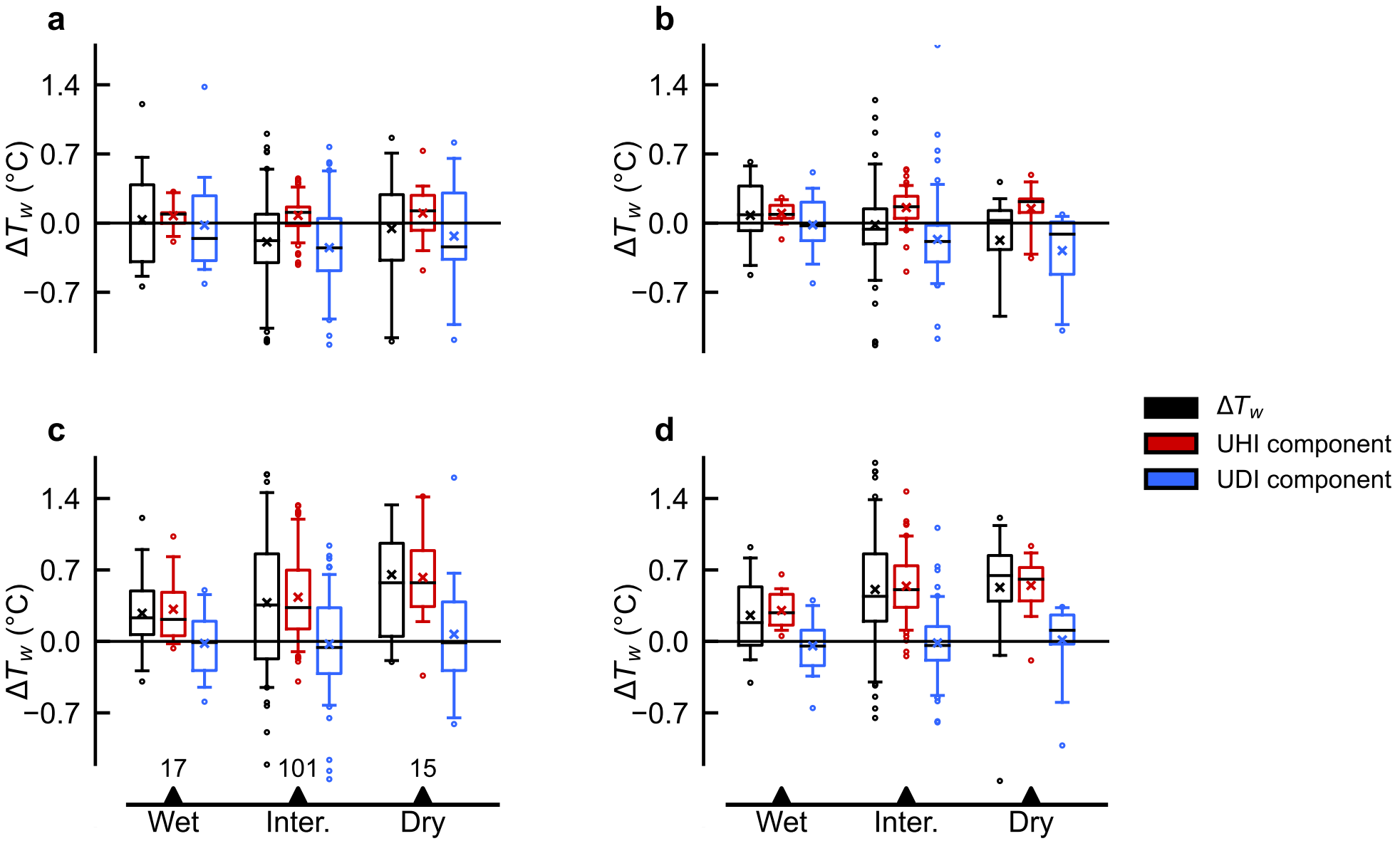
a
b
c
d
1.4
0.7
0.0
−0.7
ΔTw (°C)
17
101
15
Wet
Inter.
Dry
ΔTw
UHI component
UDI component

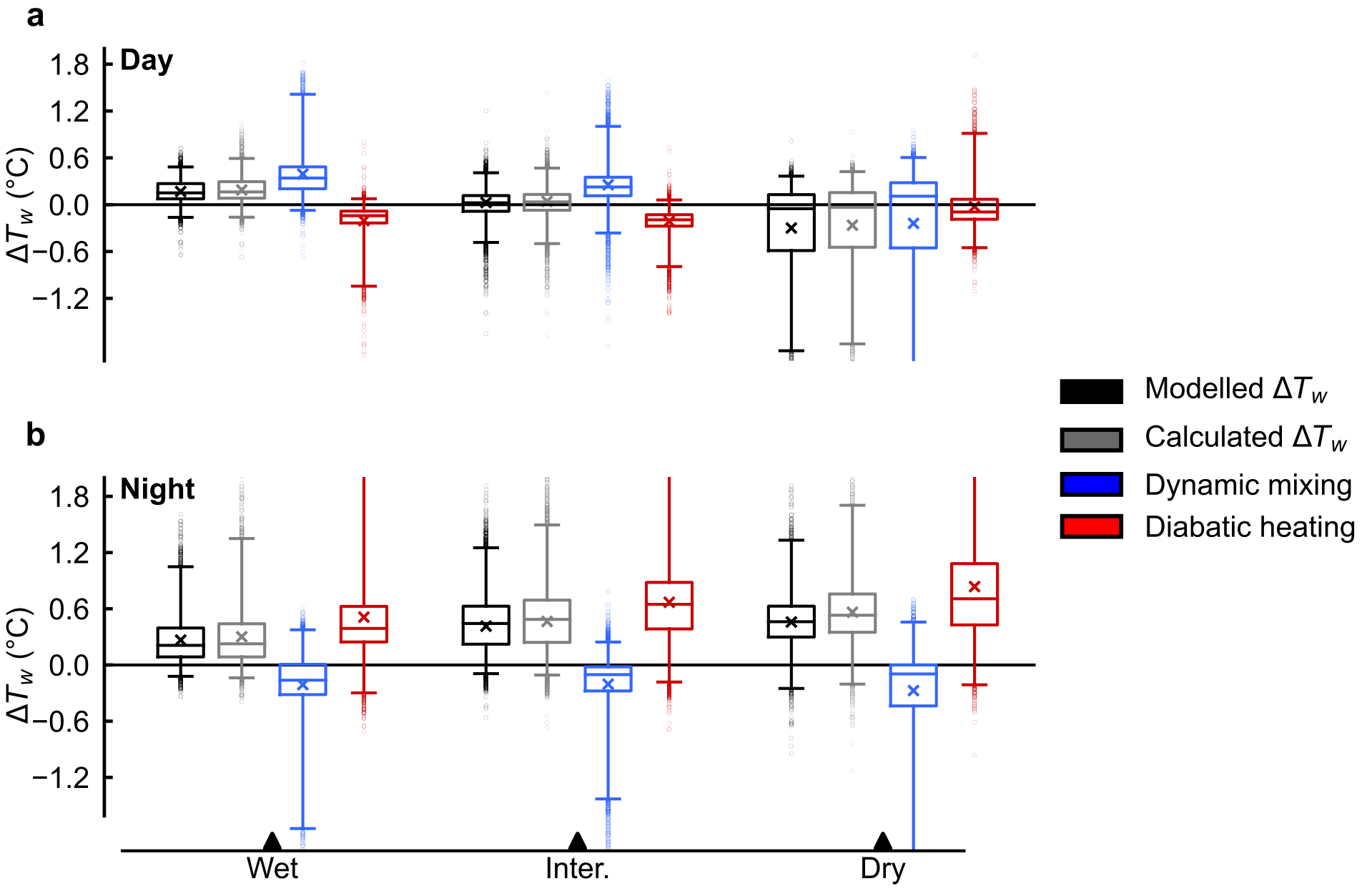
a
Day
1.8
1.2
0.6
0.0
−0.6
−1.2
ΔTw (°C)
b
Night
1.8
1.2
0.6
0.0
−0.6
−1.2
ΔTw (°C)
Wet
Inter.
Dry
Modelled ΔTw
Calculated ΔTw
Dynamic mixing
Diabatic heating

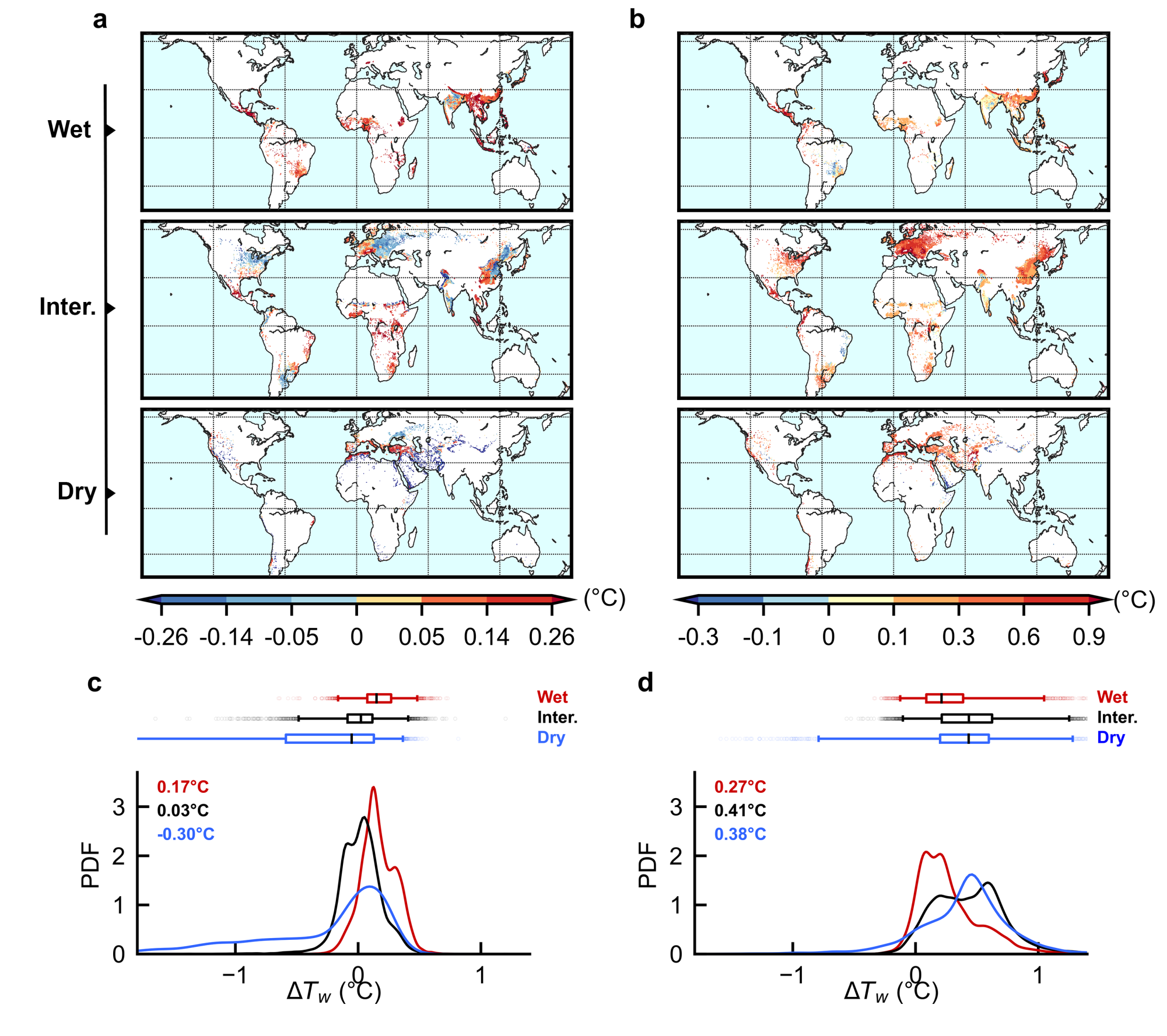
a
b
Wet
Inter.
Dry
(°C)
-0.26 -0.14 -0.05 0 0.05 0.14 0.26
(°C)
-0.3 -0.1 0 0.1 0.3 0.6 0.9
c
d
Wet
Inter.
Dry
0.17°C
0.03°C
-0.30°C
0.27°C
0.41°C
0.38°C
PDF
ΔTw (°C)

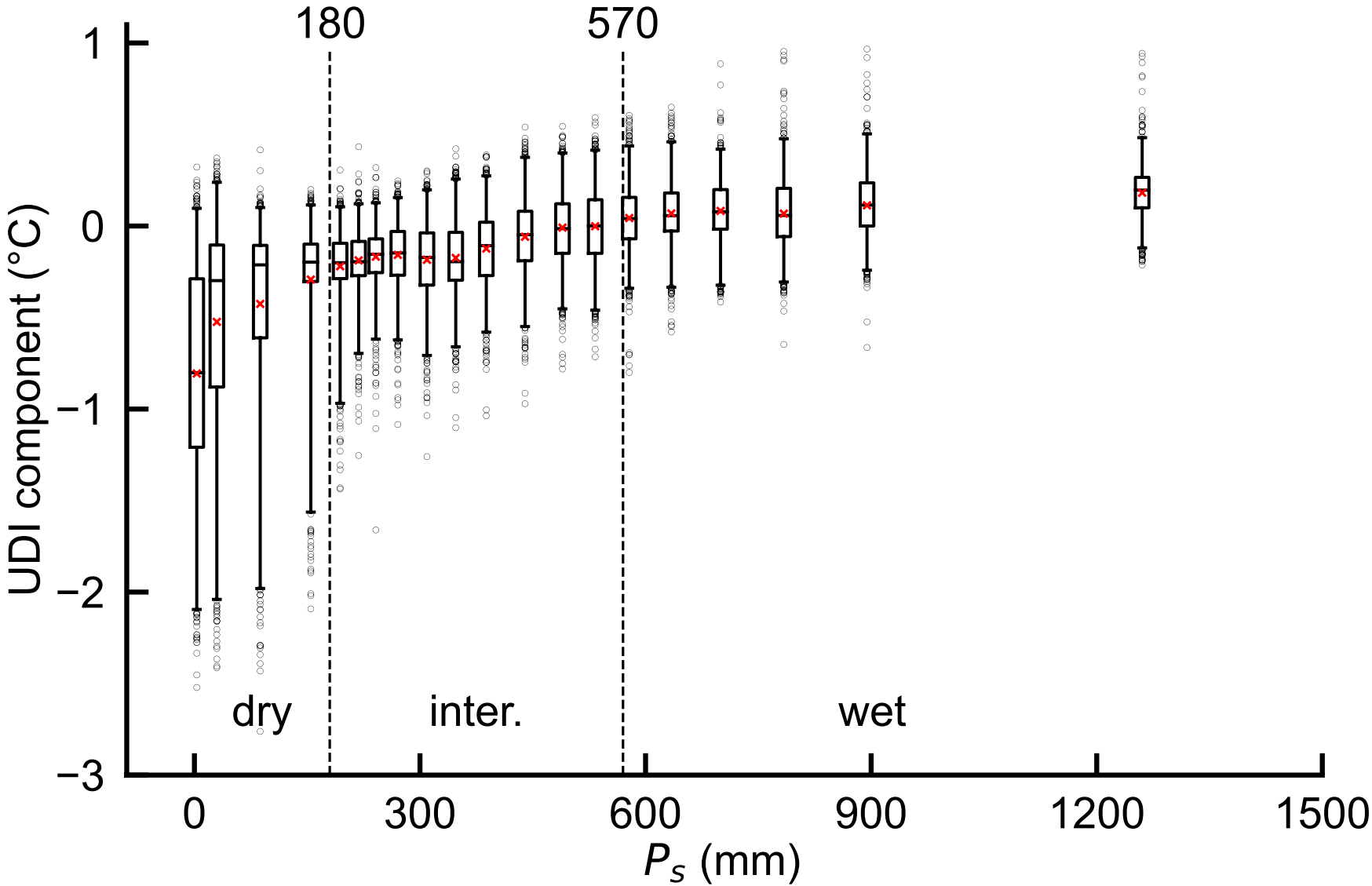
180
570
1
0
−1
−2
−3
UDI component (°C)
dry
inter.
wet
0
300
600
900
1200
1500
P_s (mm)

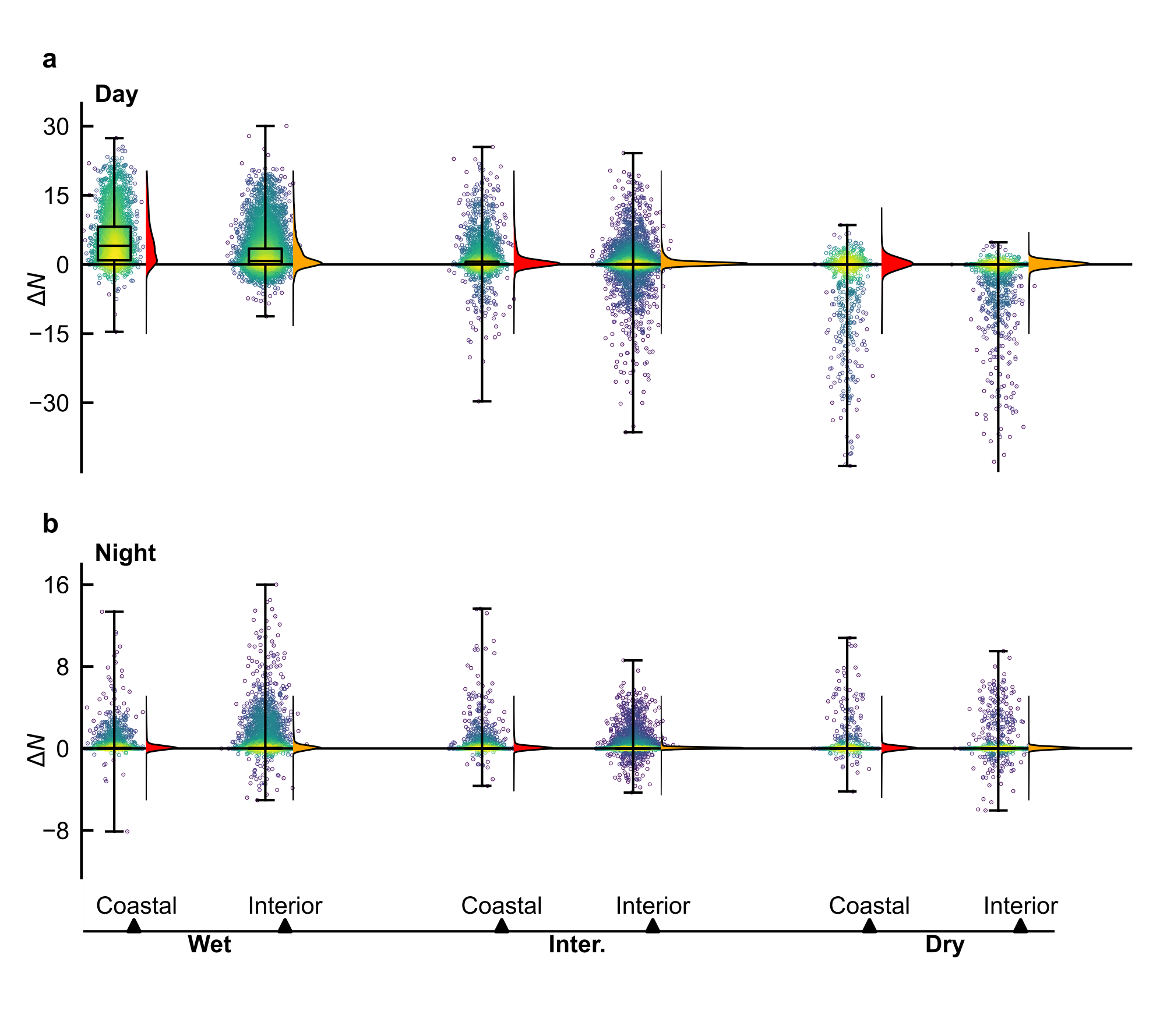
a
Day
30
15
0
−15
−30
ΔN
b
Night
16
8
0
−8
ΔN
Coastal
Interior
Coastal
Interior
Coastal
Interior
Wet
Inter.
Dry

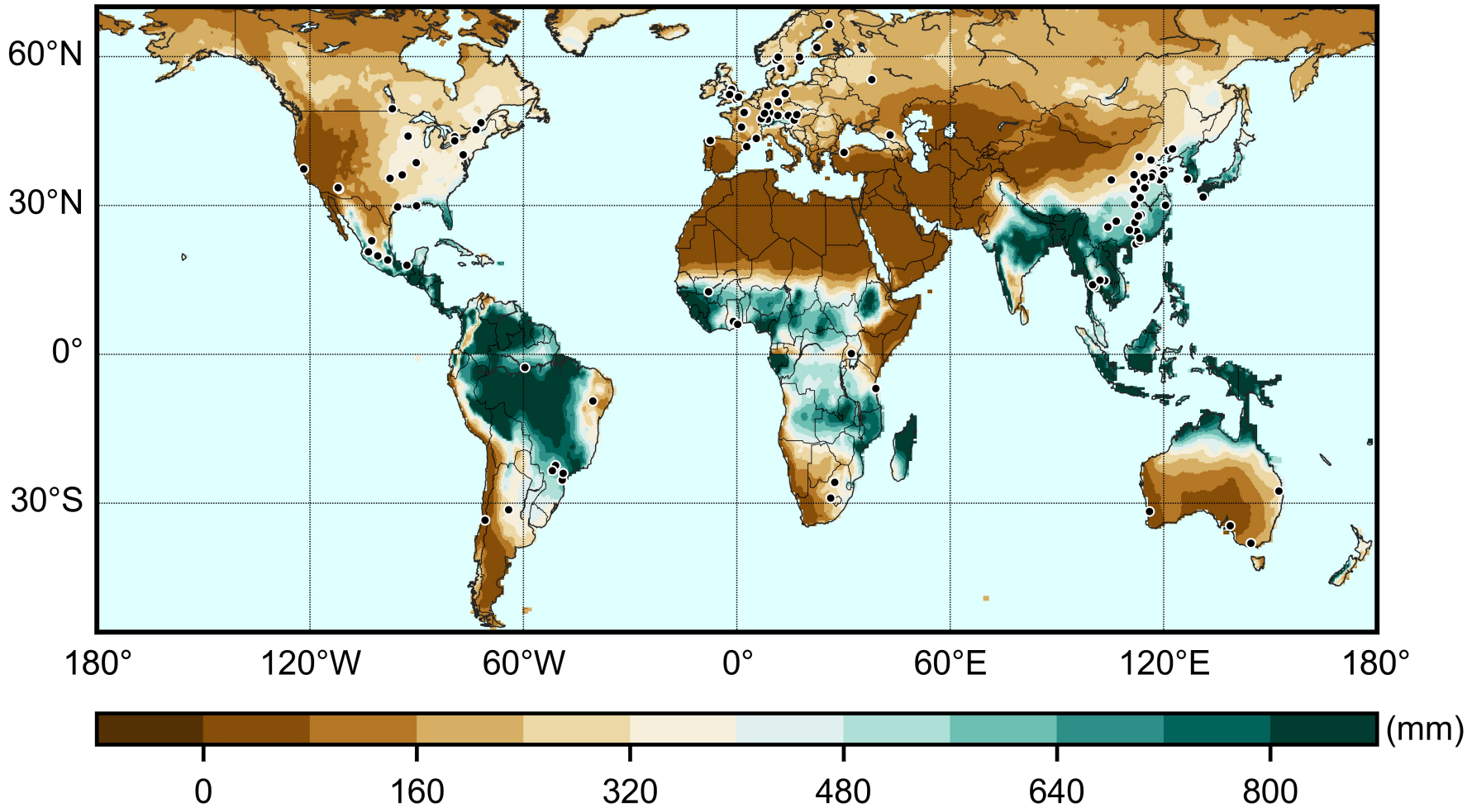
60°N
30°N
0°
30°S
180°
120°W
60°W
0°
60°E
120°E
180°
0
160
320
480
640
800
(mm)

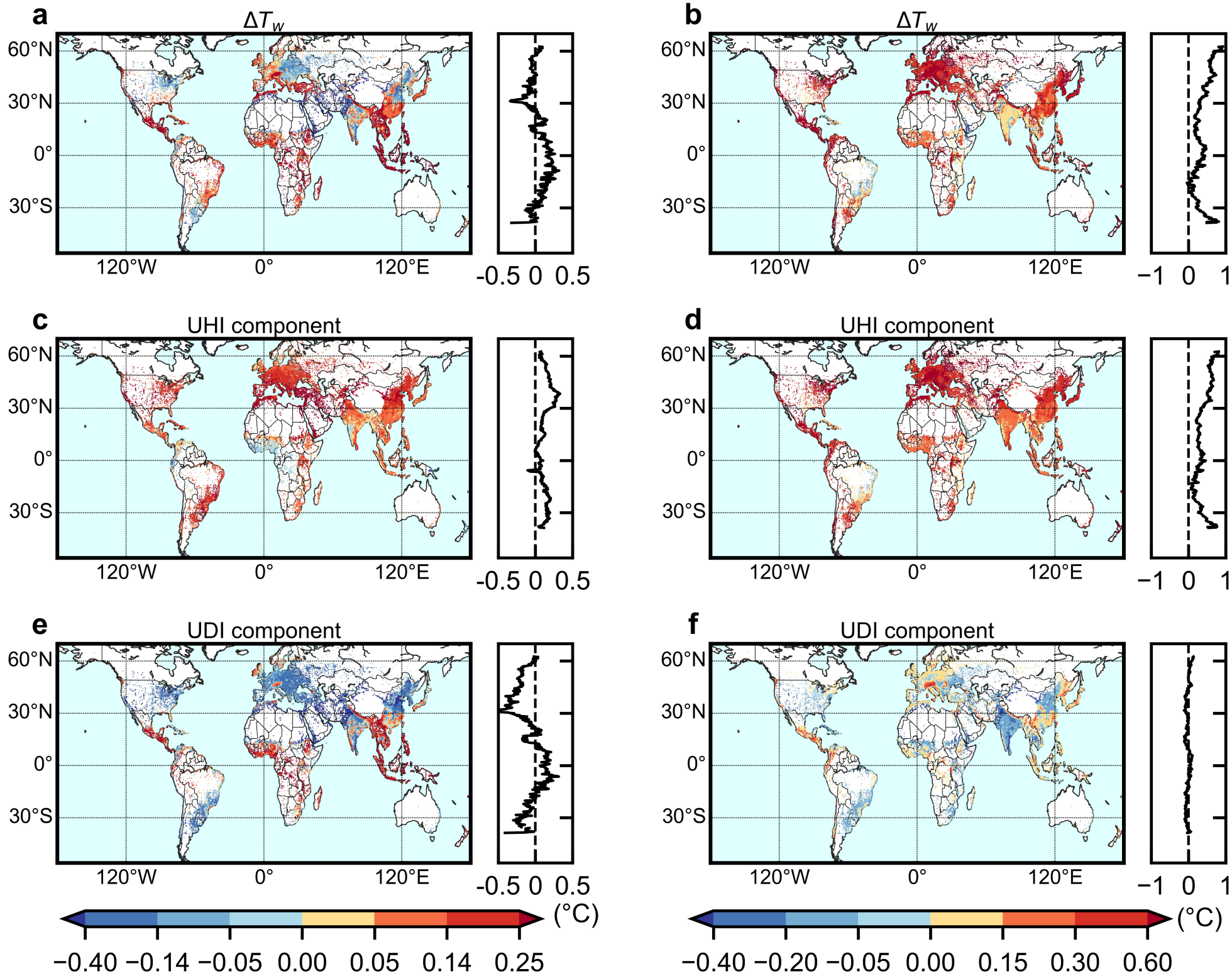
a
ΔT_w
b
ΔT_w
c
UHI component
d
UHI component
e
UDI component
f
UDI component
60°N
30°N
0°
30°S
120°W
0°
120°E
-0.5 0 0.5
−1 0 1
(°C)
−0.40 −0.14 −0.05 0.00 0.05 0.14 0.25
−0.40 −0.20 −0.05 0.00 0.15 0.30 0.60

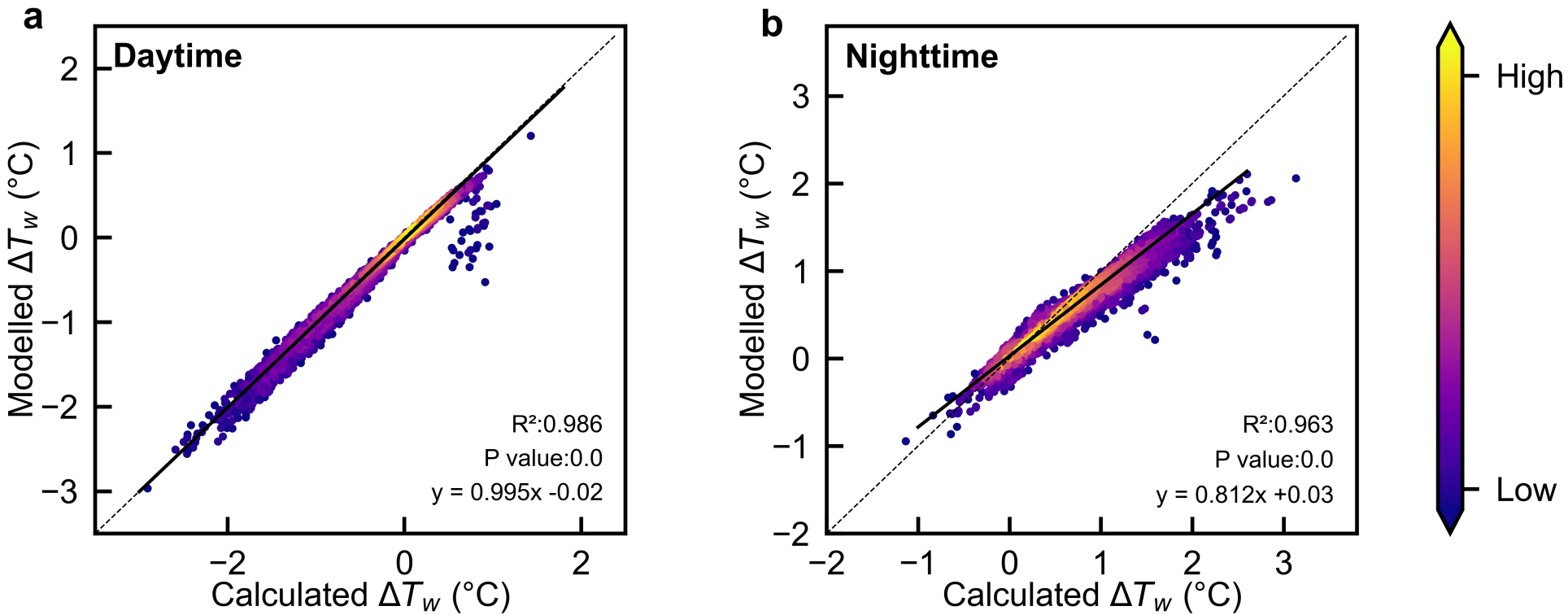
a
Daytime
Modelled ΔT_w (°C)
Calculated ΔT_w (°C)
R²:0.986
P value:0.0
y = 0.995x -0.02
b
Nighttime
Modelled ΔT_w (°C)
Calculated ΔT_w (°C)
R²:0.963
P value:0.0
y = 0.812x +0.03
High
Low

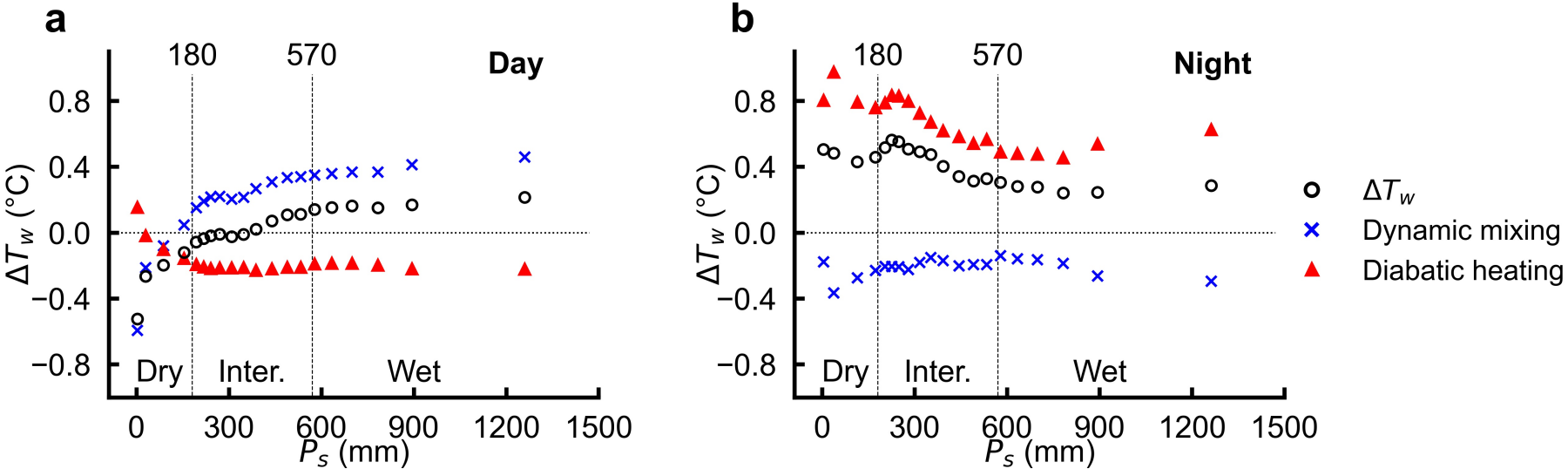
a
b
180
570
Day
Night
0.8
0.4
0.0
−0.4
−0.8
ΔT_w (°C)
Dry
Inter.
Wet
0
300
600
900
1200
1500
P_s (mm)
ΔT_w
Dynamic mixing
Diabatic heating

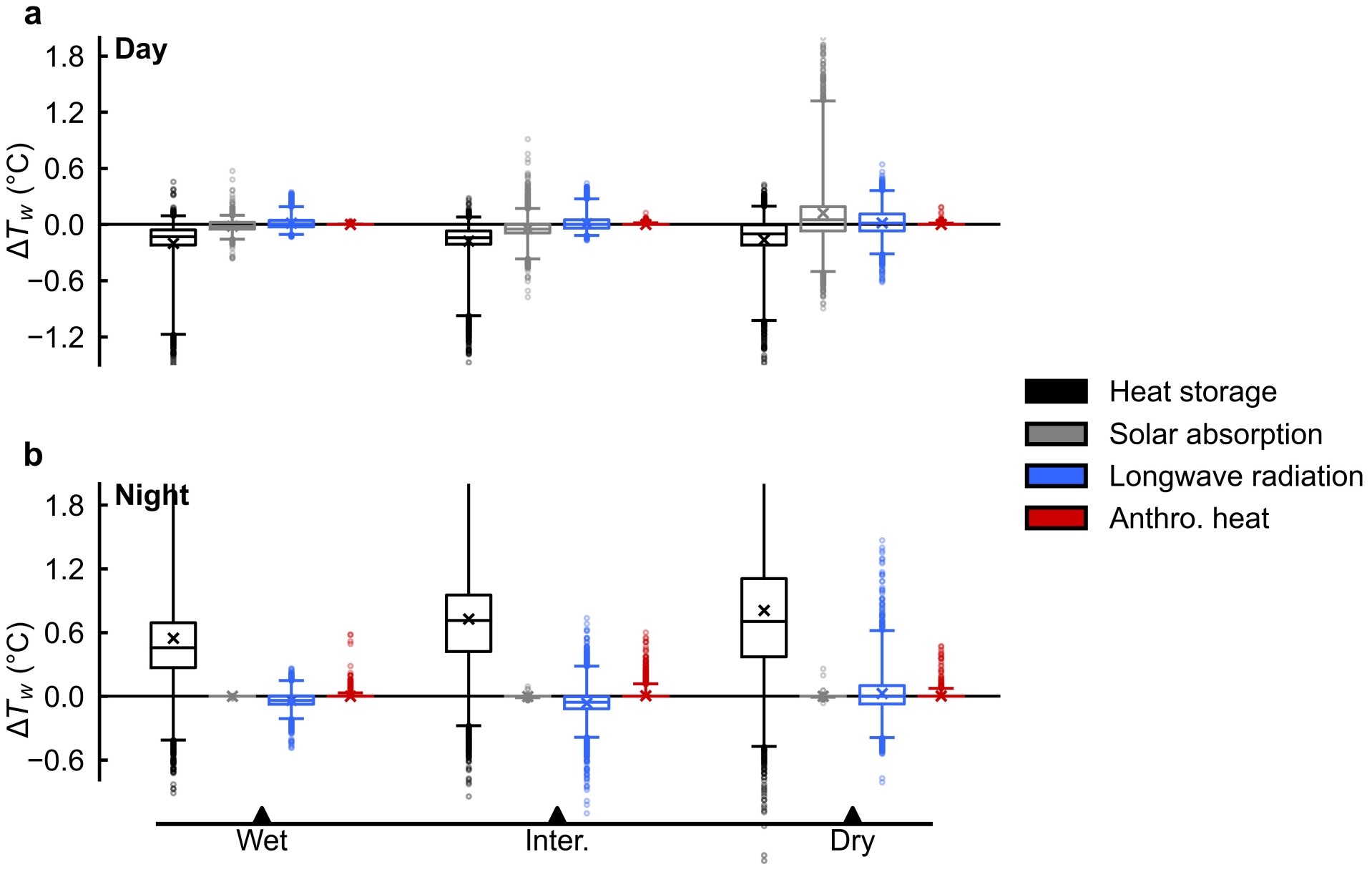
a
Day
1.8
1.2
0.6
0.0
−0.6
−1.2
ΔT_w (°C)
b
Night
1.8
1.2
0.6
0.0
−0.6
ΔT_w (°C)
Wet
Inter.
Dry
Heat storage
Solar absorption
Longwave radiation
Anthro. heat

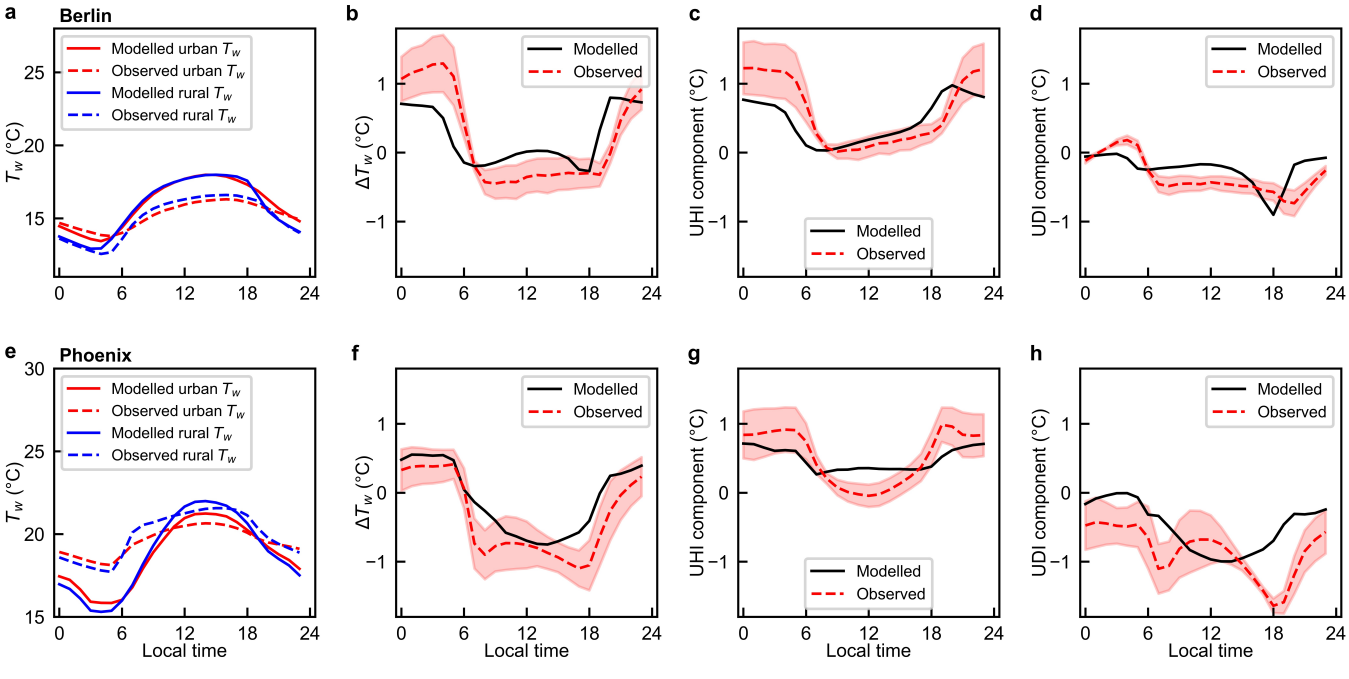
a
Berlin
Modelled urban T_w
Observed urban T_w
Modelled rural T_w
Observed rural T_w
T_w (°C)
b
Modelled
Observed
ΔT_w (°C)
c
Modelled
Observed
UHI component (°C)
d
Modelled
Observed
UDI component (°C)
e
Phoenix
Modelled urban T_w
Observed urban T_w
Modelled rural T_w
Observed rural T_w
T_w (°C)
Local time
f
Modelled
Observed
ΔT_w (°C)
Local time
g
Modelled
Observed
UHI component (°C)
Local time
h
Modelled
Observed
UDI component (°C)
Local time

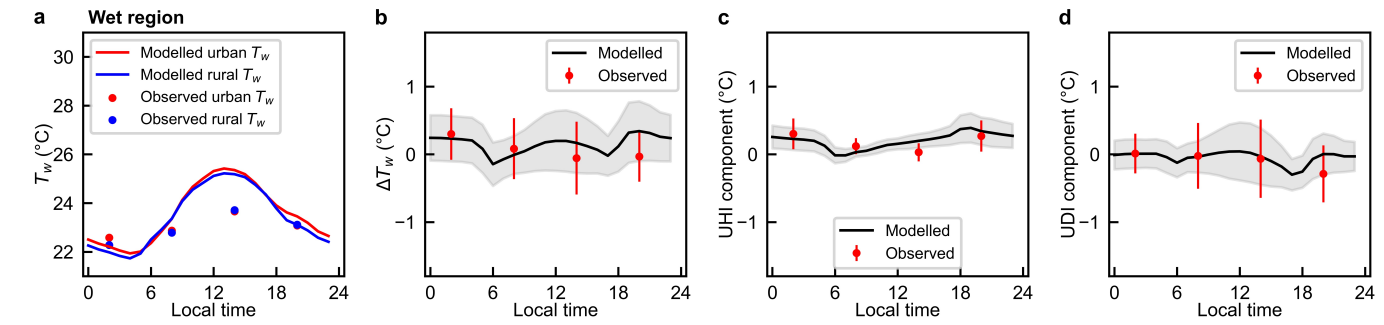
a
Wet region
Modelled urban T_w
Modelled rural T_w
Observed urban T_w
Observed rural T_w
T_w (°C)
Local time
b
Modelled
Observed
ΔT_w (°C)
Local time
c
Modelled
Observed
UHI component (°C)
Local time
d
Modelled
Observed
UDI component (°C)
Local time

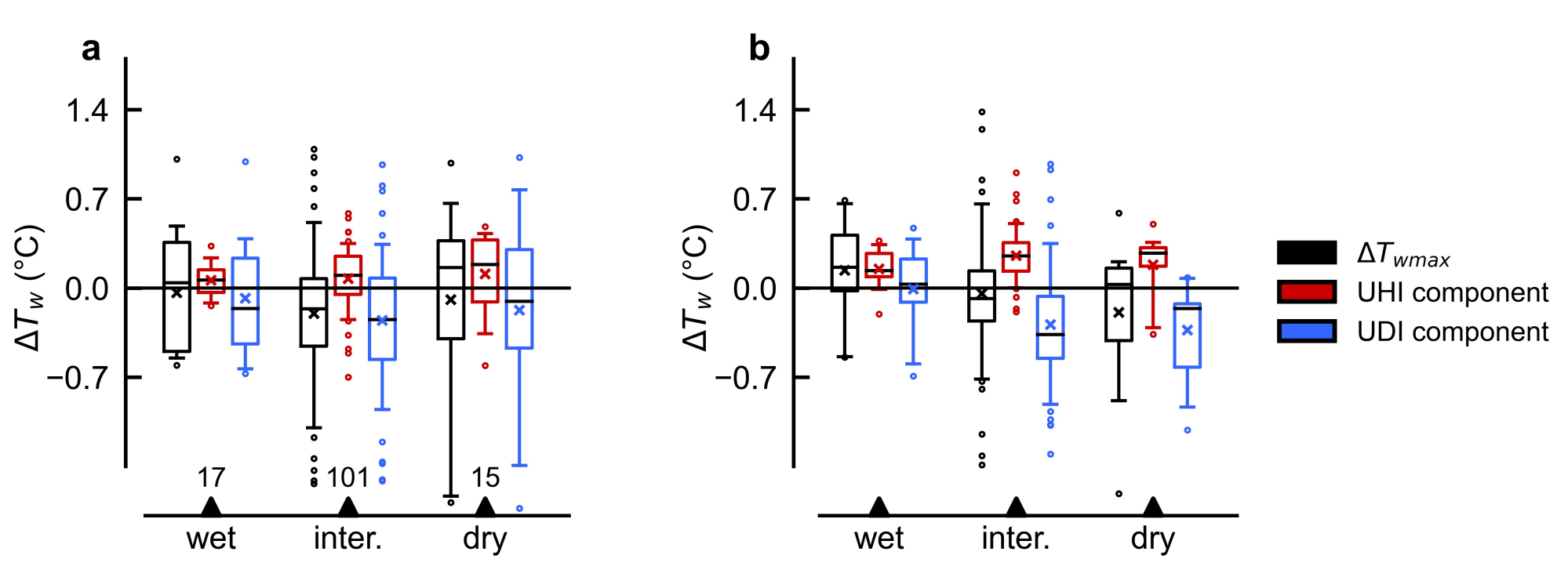
a
b
1.4
0.7
0.0
−0.7
ΔTw (°C)
17
101
15
wet
inter.
dry
ΔTwmax
UHI component
UDI component

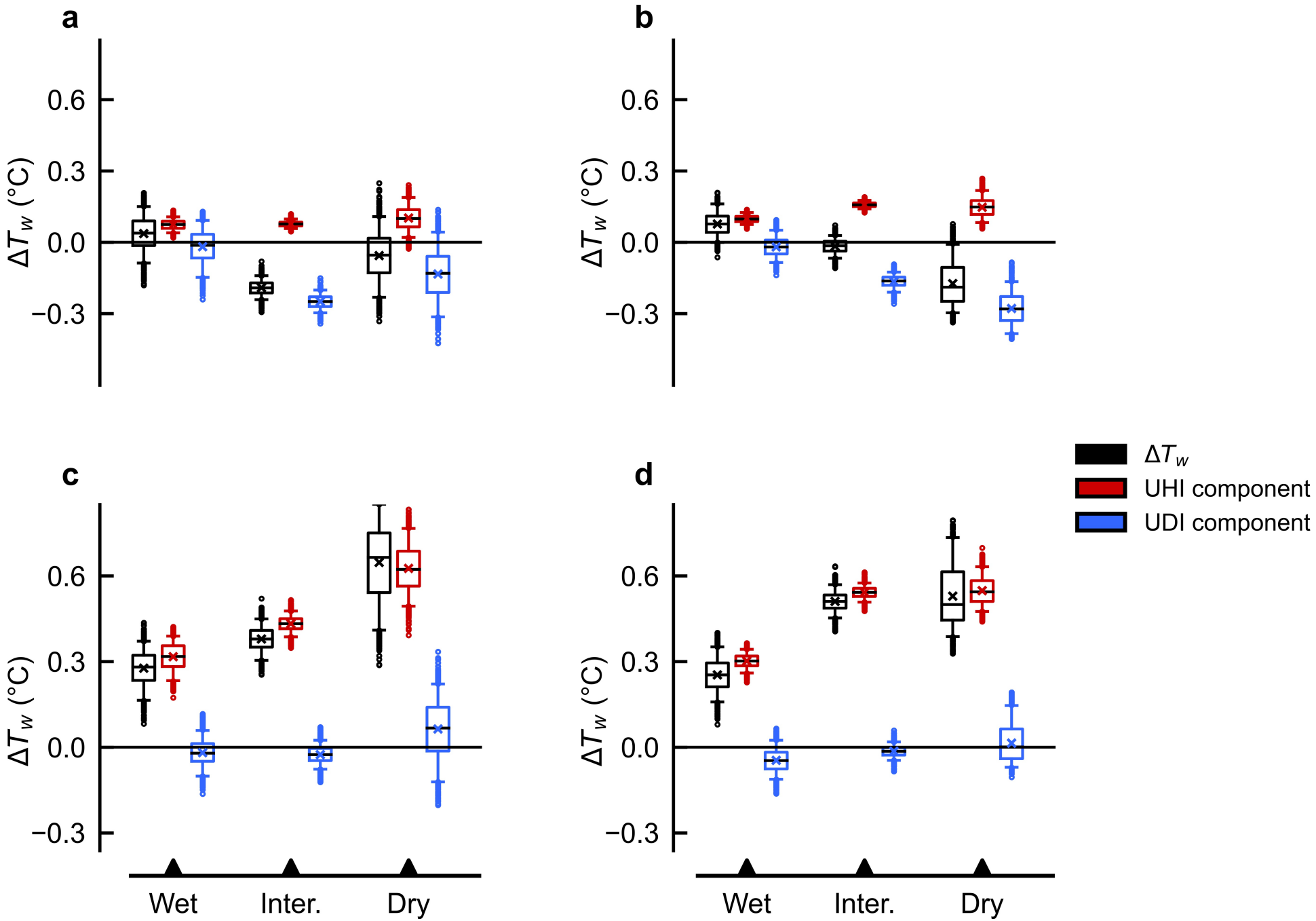
a
b
c
d
0.6
0.3
0.0
−0.3
ΔTw (°C)
Wet
Inter.
Dry
ΔTw
UHI component
UDI component

Region	Day					
	Indices	T_w	Humidex	WBGT	DI	HI
Wet	w_1	0.26	1.00	0.48	0.63	1.56
	w_2	0.26	0.37	0.18	0.13	0.45
	w_1/w_2	1.00	2.73	2.67	4.85	3.47
Inter.	w_1	0.30	1.00	0.51	0.65	1.11
	w_2	0.30	0.37	0.21	0.15	0.22
	w_1/w_2	1.00	2.73	2.43	4.33	5.05
Dry	w_1	0.32	1.00	0.52	0.66	0.83
	w_2	0.32	0.37	0.22	0.16	0.23
	w_1/w_2	1.00	2.73	2.36	4.13	3.61

Region	Night					
	Indices	T_w	Humidex	WBGT	DI	HI
Wet	w_1	0.28	1.00	0.50	0.64	2.21
	w_2	0.28	0.37	0.20	0.14	-0.24
	w_1/w_2	1.00	2.73	2.50	4.57	-9.21
Inter.	w_1	0.34	1.00	0.53	0.67	1.68
	w_2	0.34	0.37	0.23	0.17	-0.38
	w_1/w_2	1.00	2.73	2.30	3.94	-4.42
Dry	w_1	0.37	1.00	0.56	0.68	0.75
	w_2	0.37	0.37	0.26	0.18	-0.10
	w_1/w_2	1.00	2.73	2.15	3.78	-7.50